Appl. Magn. Reson. 31, 29–43 (2007)

Applied Magnetic Resonance

Light-Induced EPR Spectra of Reaction Centers from *Rhodobacter sphaeroides* at 80 K: Evidence for Reduction of Q_B by B Branch Electron Transfer in Native Reaction Centers

M. L. Paddock, R. A. Isaacson, E. C. Abresch, and **M. Y. Okamura**

Department of Physics, University of California, San Diego, California, USA

Received August 28, 2006; revised September 16, 2006

Abstract. Photosynthetic reaction centers (RCs) from *Rhodobacter sphaeroides* capture solar energy by electron transfer from primary donor D to quinone acceptor Q_B through the active A branch of electron acceptors, but not the inactive B branch. The light-induced electron paramagnetic resonance (EPR) spectrum from native RCs that had Fe^{2+} replaced by Zn^{2+} was investigated at cryogenic temperature (80 K, 35 GHz). In addition to the light-induced signal due to the formation of $D^{+\bullet}Q_A^{-\bullet}$ observed previously, a small fraction (ca. 5%) of the signal displayed very different characteristics. The signal was absent in RCs in which the Q_B was displaced by the inhibitor stigmatellin. Its decay time ($\tau = 6$ s) was the same as observed for $D^{+\bullet}Q_B^{-\bullet}$ in mutant RCs lacking Q_A, which is significantly slower than for $D^{+\bullet}Q_A^{-\bullet}$ ($\tau = 30$ ms). Its EPR spectrum was identical to that of $D^{+\bullet}Q_B^{-\bullet}$. The quantum efficiency for forming the major component of the signal was the same as that found for mutant RCs lacking Q_A ($\Phi = 0.2\%$) and was temperature independent. These results are explained by direct photochemical reduction of Q_B via B branch electron transfer in a small fraction of native RCs.

1 Introduction

The primary photochemistry in bacterial photosynthesis involves light-induced electron transfer from an electron donor D to an electron acceptor A in a membrane-bound protein called the reaction center (RC) [1]. In this process, light illumination produces relatively stable free radical species with high quantum efficiency according to the following equation:

$$DA + h\nu \rightleftarrows D^{+\bullet}A^{-\bullet}. \quad (1)$$

Over the past 40 years, results from magnetic resonance studies helped identify the primary electron transfer species in RCs and elucidate the mechanisms of electron transfer [2–5]. In the bacterial RC, the light-induced signals were observed from the oxidized donor $D^{+\bullet}$ [6, 7] and the reduced acceptor $A^{-\bullet}$ [7,

8]. The donor species $D^{+\bullet}$ had an electron paramagnetic resonance (EPR) spectrum similar to bacteriochlorophyll $BChl^{+\bullet}$ ($g = 2.0026$). However, both the EPR line width [9] and electron–nuclear double resonance (ENDOR) splittings were smaller [10], indicating delocalization of the unpaired electron over a dimer of BChl molecules [9]. The EPR spectrum of the acceptor $A^{-\bullet}$ observed only at cryogenic temperatures [7] was orders of magnitude broader and centered near $g = 1.8$. Upon removing the Fe^{2+}, the signal shifted to $g = 2.0045$ with a narrow line width (ca. 10 G) and was shown to be due to ubisemiquinone, $Q_A^{-\bullet}$ [11, 12]. The earlier observed broader EPR signal was shown to result from the magnetic coupling of $Q_A^{-\bullet}$ with the neighboring high-spin Fe^{2+} [13]. A second weakly bound ubisemiquinone $Q_B^{-\bullet}$, also magnetically coupled to Fe^{2+}, could also be observed [13, 14] if RCs were illuminated at room temperature before freezing but was not observed by illumination at cryogenic temperature [13]. These results can be explained by a pathway of electron transfer from the excited donor D^* to electron acceptor Q_A followed by electron transfer from $Q_A^{-\bullet}$ to Q_B, where the electron transfer from $Q_A^{-\bullet}$ to Q_B is inhibited at cryogenic temperatures. When RCs were illuminated at cryogenic temperatures, the formation and decay of the $D^{+\bullet}Q_A^{-\bullet}$ state was observed [15, 16]. The signal decayed with a time constant ($\tau_D = 1/k_D = 30$ ms) that was almost temperature-independent and indicative of an electron tunneling mechanism for the $D^{+\bullet}Q_A^{-\bullet} \rightarrow DQ_A$ recombination reactions. In the present work, we extend low-temperature EPR kinetic experiments and examine the properties of a new light-induced EPR signal that demonstrates an alternate pathway for electron transfer to Q_B.

The structure of the electron transfer cofactors in *Rhodobacter sphaero-ides* RCs obtained by X-ray crystallography [17] is shown in Fig. 1. Four bacteriochlorophyll, two bacteriopheophytin, two ubiquinone molecules and a non-heme Fe^{2+} ion are arranged in pseudo-symmetrical branches (A branch and B branch) extending across the protein (Fig. 1). Although the two branches are structurally similar, they differ dramatically in their electron transfer activities [18]. Photochemical electron transfer proceeds almost exclusively along the active A branch, from a primary electron donor, D, through a bacteriochlorophyll and bacteriopheophytin, to a bound quinone, Q_A (Fig. 1). The reduction of Q_A occurs rapidly ($\tau \sim 0.2$ ns) with a quantum yield of 98% [19], has a rate of formation that is almost temperature independent and proceeds even at cryogenic temperatures. Subsequent electron transfer from $Q_A^{-\bullet}$ to a secondary quinone Q_B is more complex [20, 21]. It occurs on a slower time scale ($\tau \sim 100$ μs) [22], is temperature dependent and does not proceed at cryogenic temperature if the RCs are frozen in the dark [23, 24]. The reaction does proceed at cryogenic temperature if the RCs are cooled in the light, i.e., in the charge-separated state [24–26]. Additionally, the rate of the reaction is driving-force independent [27]. These results are consistent with the electron transfer reaction being governed by a conformational gating process. The complete reduction of Q_B to Q_BH_2 requires a second photochemically initiated electron transfer from $Q_A^{-\bullet}$ that is coupled with the binding of two protons. In intact membranes, Q_BH_2 dissociates from the RC, diffuses to the cytochrome bc_1 complex and upon oxidation

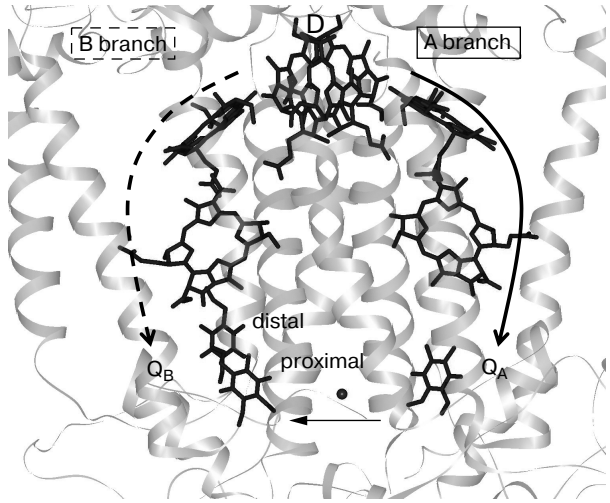

Fig. 1. Structure of the cofactors in *R. sphaeroides* RCs (based on coordinates 1AIG and 1AIJ [17]. Electron transfer occurs with high efficiency along the A branch (solid arrow). Following light excitation, electron transfer occurs from the excited state of the donor D to the primary quinone electron acceptor Q_A. This transfer occurs even at cryogenic temperature. Electron transfer from $Q_A^{-\bullet}$ to Q_B is temperature dependent and inhibited at cryogenic temperatures. Two positions for Q_B, distal and proximal, are indicated; their properties are discussed in the text. Possible electron transfer along the B branch (dotted arrow) with low quantum yield is the focus of this study.

releases the protons across the membrane to provide a proton gradient that drives ATP synthesis [1].

Although the B branch is not the main pathway for electron transfer to Q_B in native RCs, recent studies indicated that direct photochemical electron transfer to Q_B can be observed [28–31] in RCs lacking Q_A. Electron transfer to Q_B presumably through the B branch [32] was observed with a quantum efficiency of 0.4% at room temperature [31]. Higher quantum efficiencies have been observed in RCs with mutations that bias electron transfer toward the B branch (reviewed in ref. 30). In mutant RCs lacking Q_A, electron transfer to Q_B has been observed at cryogenic temperatures [33]. The charge recombination from the $D^{+\bullet}Q_B^{-\bullet}$ state in these RCs at 80 K has been found to be 5 ± 1 s for RCs frozen in the dark. In native RCs, direct photochemical electron transfer to Q_B has not been observed, possibly due to the inability of the B branch to compete with electron transfer through the highly efficient A branch. In this work, we measured EPR in native RCs frozen in the dark (80 K) to specifically investigate whether any photochemical reduction of Q_B via the B branch was observable. Since the electron transfer reaction from $Q_A^{-\bullet}$ to Q_B is blocked at cryogenic temperatures, we expected that Q_B reduction at cryogenic temperatures would require electron transfer via the less efficient B branch. EPR spectroscopy was used to monitor both the decay kinetics of the charge-separated state following illumination and the spectrum of the radicals formed in the charge-separated state.

These properties were measured at different illumination intensities and for different illumination times. Two EPR components were observed – one indicative of $D^{+\bullet}Q_A^{-\bullet}$ which decayed within 30 ms and another one of a longer-lived state. Since the charge-separated states had different lifetimes and quantum efficiencies, the relative population was dependent on the light intensity. Thus, the EPR spectrum of the longer-lived state was determined. The results and implications for B branch electron transfer in the native RC are discussed.

2 Materials and Methods

RC purification and biochemical Zn^{2+} replacement. RCs were purified as previously described [34]. To perform EPR studies, the high-spin Fe^{2+} was removed and replaced with diamagnetic Zn^{2+} as described by Debus et al. [35] and as modified by Utschig et al. [36]. The RCs were reconstituted with about 3-fold excess of deuterated ubiquinone 10 (Q_{10}) in 1% lauryldimethylamino-N-oxide to occupy the Q_B site followed by dialysis against TMK (2 mM Tris-HCl, pH 8, 0.04% β-D-maltoside, 5 mM KCl).

35 GHz EPR measurements. EPR spectroscopy was performed at a microwave frequency of 35.03 GHz at $T = 80$ K as previously described [37]. EPR spectra were measured using field modulation ($f = 270$ Hz, ΔH(peak to peak) = 1.5 G). Kinetic measurements were made using a larger modulation field (ΔH(peak to peak) = 5–10 G). Typically, the data from 10–100 traces were averaged. RCs were concentrated and diluted 1:10 into D_2O. RCs were concentrated to about 100 μM for sample preparation. In control samples, stigmatellin was added to inhibit Q_B activity. A tungsten lamp was used to illuminate the sample in the magnetic resonance cavity to generate the charge-separated state (water filter, $I = 0.1$ W/cm^2 at full intensity). The incident light was modulated using an electromechanical shutter. The light intensity was varied by inserting partially transmitting neutral-density screens into the light path.

3 Results

3.1 Light-Induced EPR Spectra

The light-induced EPR spectra were studied by illumination of the dark-frozen RC samples in the EPR spectrometer. In these samples, the high-spin Fe^{2+} was replaced with the diamagnetic Zn^{2+} to prevent broadening of the $Q^{-\bullet}$ signal and the RCs were reconstituted with deuterated Q_{10} in D_2O buffer to further narrow the EPR line width. The EPR spectra of the sample in the dark and under illumination are shown in Fig. 2 ($T = 80$ K; frequency, 35.03 GHz). The light-induced spectrum is a superposition of the spectra expected for the donor radical $D^{+\bullet}$ and semiquinone $Q^{-\bullet}$ [2, 5]. The low-field peak is due to the g_x component of ubisemiquinone, $Q^{-\bullet}$. The central peak is predominantly due to $D^{+\bullet}$; the peak

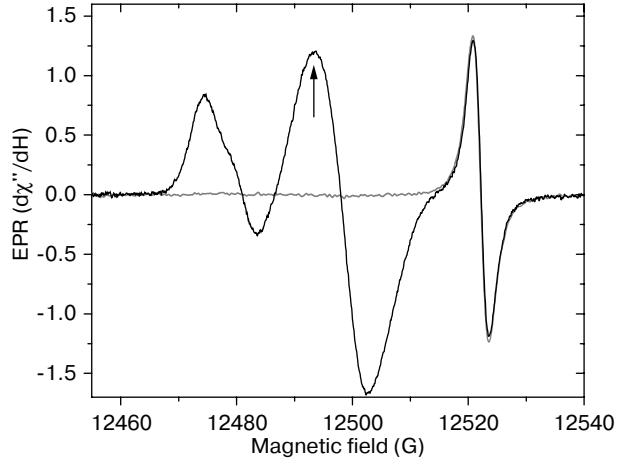

Fig. 2. EPR spectrum of RCs frozen in the dark ($T = 80$ K, $\nu = 35.03$ GHz). The dark heavy line is the spectrum generated by illumination of the RCs in the EPR cavity. The lowest magnetic field peak is due to the ubisemiquinone $Q^{-\bullet}$; the middle field peak to contributions from the oxidized donor $D^{+\bullet}$ (predominant), and the reduced acceptor $Q^{-\bullet}$ (lesser); and the high-field peak a g-marker ($g = 1.99891$). The baseline spectrum before illumination is shown (thinner grey line). The arrow indicates the magnetic field position used for the kinetic studies. (Conditions: 100 μM RCs in TMK and D_2O; 80 K; $\nu = 35$ GHz; magnetic field modulation [$f = 270$ Hz, $\Delta H = 1.5$ G]; average 28 traces; time constant, 20 ms; scan time, 30 s.)

contains a minor contribution (ca. 10%) from $Q^{-\bullet}$. The high-field peak is due to a g-marker ($g = 1.99891$).

3.2 Formation and Decay Kinetics of the Light-Induced Signal

The amplitude of the EPR signal of the sample was measured at 80 K as a function of time preceding, during and following illumination. Figure 3a shows the EPR signal measured at the middle peak (12493 G) predominantly due to $D^{+\bullet}$ at the highest light intensity ($I = 100\%$, ca. 0.1 W/cm^2 at the sample). The amplitude of the EPR signal increased rapidly when the light was turned on and decayed rapidly when the light was turned off. The fast decay had a time constant $\tau_f = 30$ ms (not resolved in this trace) as found previously for the decay of $D^{+\bullet}Q_A^{-\bullet} \rightarrow DQ_A$ [16]. However, a second slower decaying phase was also observed (arrow in Fig. 3a). This slow decay accounted for 5% of the signal and had a longer time constant $\tau_s = 6 \pm 1$ s. When the sample was illuminated at lower light intensity, the relative amplitude of the slow phase was larger. The relative amplitude increased to about 40% when the light intensity was reduced 50-fold to 2% of the maximal light intensity (Fig. 3b). This was the consequence of an about 5-fold larger decrease in the amplitude of the fast phase compared with the slow phase. This shows that the two signals have different light saturation behaviors.

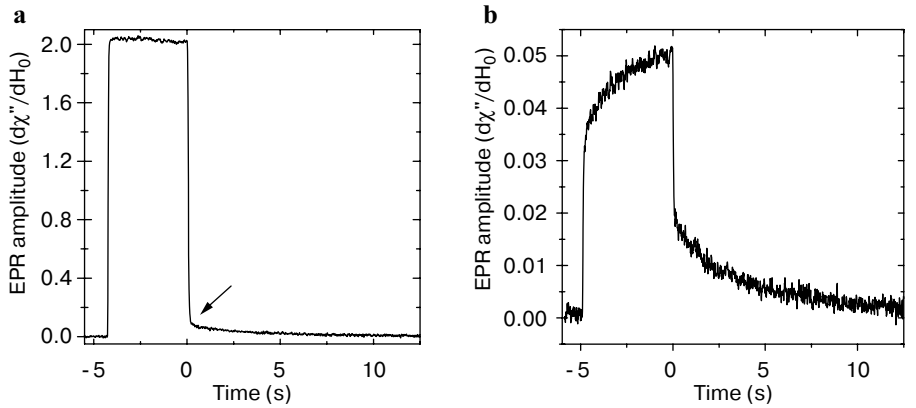

Fig. 3. Formation and decay kinetics of the light-induced EPR signal of $D^{+\bullet}Q^{-\bullet}$ at higher light intensity ($I = 100\%$) (**a**), and at lower light intensity ($I = 2\%$) (**b**). The sample is illuminated from $t = -4$ s to $t = 0$ s. At high light intensity the decay of the signal consists of a fast phase ($\tau = 30$ ms, unresolved in this trace) that has been previously reported [15]. In addition a slow phase with decay time ($\tau = 6.0 \pm 1$ s) that represents about 5% of the amplitude is also seen (arrow). The two kinetic phases are more apparent at lower light intensity (**b**) due the decrease in amplitude of the fast phase relative to that of the slow phase. In addition, a slow phase in the rise of the signal is also apparent. The amount of the slowly decaying component was equal to that of the slowly rising component. (Conditions: same as for Fig. 2, magnetic field fixed at 12493 G, field modulation $\Delta H = 10$ G, average of 10–100 traces.)

The same kinetics were observed when monitoring the EPR signal at the lower peak position due to $Q^{-\bullet}$ (12482 G) This shows that the slow phase is due to the decay of a $D^{+\bullet}Q^{-\bullet}$ species (either $D^{+\bullet}Q_A^{-\bullet}$ or $D^{+\bullet}Q_B^{-\bullet}$). At the lower light intensity, the kinetics of the formation of the EPR signal was also more clearly biphasic. The amplitude of the slowly rising phase was comparable to the amplitude of the slowly decaying phase.

To test whether the amplitudes were correlated, the kinetic rise and decay was measured after different times of illumination (Fig. 4). The amplitude of the slowly rising phase was equal to the amplitude of the slowly decaying phase (with the same $\tau_s = 6$ s) for all illumination times. This shows that the same charge-separated state gives rise to both the slowly rising and the slowly decaying phases.

Interestingly, the time constant (6 ± 1 s) observed for the slow phase was the same within the uncertainty as that observed in RC lacking Q_A ($\tau = 5 \pm 1$ s) attributed to the decay of the $D^{+\bullet}Q_B^{-\bullet}$ state [33]. In order to test whether the slow phase in the native RC is also due to the decay of $D^{+\bullet}Q_B^{-\bullet}$, we added stigmatellin, an inhibitor which displaces Q_B from its binding site [38]. The amplitudes of both slowly rising and slowly decaying components were decreased more than 30-fold, to the level of the noise. This was most apparent at low light intensity (2%) (Fig. 5) since the relative amplitudes of the slow phases is greater. This shows that the slowly rising and decaying components are due to the formation and decay of the $D^{+\bullet}Q_B^{-\bullet}$ state.

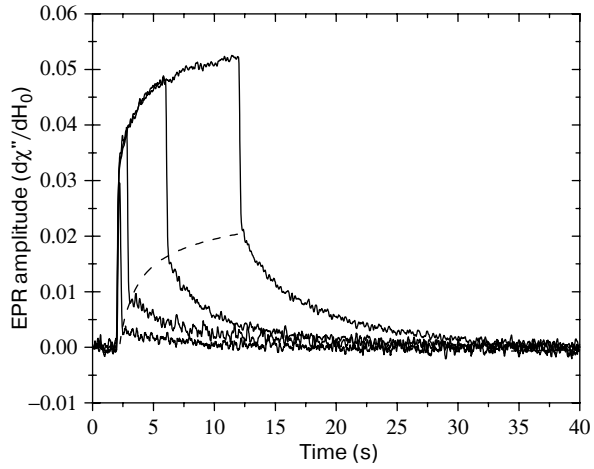

Fig. 4. Dependence of fast and slow phase amplitudes on illumination time. The illumination time was varied at low light intensity (2%). The amplitude of the slowly decaying component increases with illumination time, while that of the fast phase is relatively constant. This indicates the quantum yield for the slow component is less than that for the fast component. The amplitude of the slower rising component is the same as that of the slower decaying component, showing that the slow rise and slow decay are properties of the same charge-separated state. (Conditions, same as for Fig. 3.)

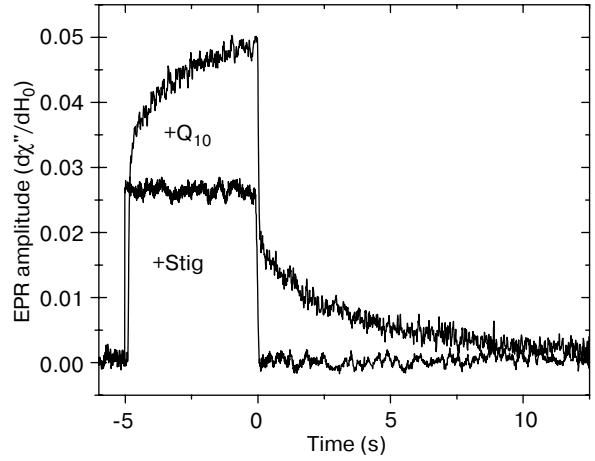

Fig. 5. Effect of stigmatellin on the slow phase. Kinetic traces are shown for the light-induced EPR signals of RCs to which either excess Q_{10} or stigmatellin (Stig) was added ($I = 2\%$). The RCs containing stigmatellin lack the slowly rising and slowly decaying phases seen in RCs having added Q_{10}. Since stigmatellin is a potent inhibitor of Q_B function, these results show that the slow rise and decay kinetic phases are due to Q_B reduction and oxidation. The time scales of the two traces are slightly displaced for better viewing. (Conditions, same as for Fig. 3.)

To test whether the formation was thermally activated, we measured the signal at different light intensities at 170 K (not shown). The relative amplitudes and decay times were the same as at 80 K, indicating that the rate of formation of the slower decaying component is not temperature dependent.

3.3 EPR Spectra of the Radicals Responsible for the Slow Kinetic Phase

To provide further support for the proposal that the slow kinetic phases are due to electron transfer involving $Q_B^{-\bullet}$, the EPR spectrum of the slow-phase reaction product was measured. In particular, the lower field region is diagnostic since the g_x value of $Q_A^{-\bullet}$ and $Q_B^{-\bullet}$ differ by several Gauss [5]. The spectrum of the unknown $Q_X^{-\bullet}$ was deconvoluted from the measured spectra by comparing higher and lower light intensity EPR spectra since the relative contribution of $Q_X^{-\bullet}$ differed. The normalized light-induced spectra at high and low light intensities are shown in Fig. 6; the traces were normalized to the middle peak that is due mostly to the EPR signal from $D^{+\bullet}$. Small differences in the low-field peak positions due to the semiquinone acceptor were observed. To obtain the spectrum of the $Q_X^{-\bullet}$, formed in the more slowly rising (and decaying) phases, the known $Q_A^{-\bullet}$ contribution was removed from the observed spectrum. This was accomplished as follows: (i) the high-light EPR spectrum (due to $Q_A^{-\bullet}$) was normalized using the $D^{+\bullet}$ signal to that at low light intensity (Fig. 6); (ii) the fraction of the fast-decaying (due to $D^{+\bullet}Q_A^{-\bullet}$) component of the 2% maximum intensity spectra was determined from the fraction of fast recombination (60% with fast decay, Fig. 3); (iii) the scaled "$Q_A^{-\bullet}$" EPR component

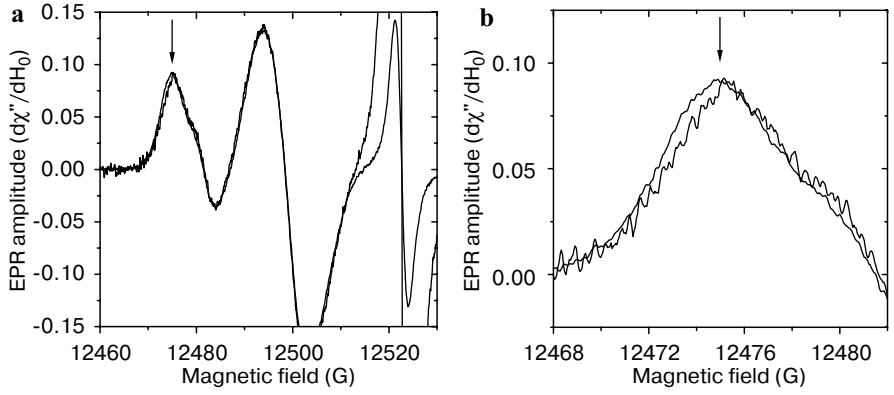

Fig. 6. EPR spectra at high (100%) and low light (2%) intensities. **a** The spectra of $D^{+\bullet}$ and $Q^{-\bullet}$ are normalized to the $D^{+\bullet}$ peak (middle). A small shift in the $Q^{-\bullet}$ spectrum (around the arrow) is observed. **b** The scale is expanded to better illustrate the observed shift in the spectrum of the $Q^{-\bullet}$ peak. The spectrum at low light intensity can be identified by its lower signal-to-noise ratio. (Conditions: same as for Fig. 2, average of 28 traces for 100% transmission and 160 traces for 2% transmission.)

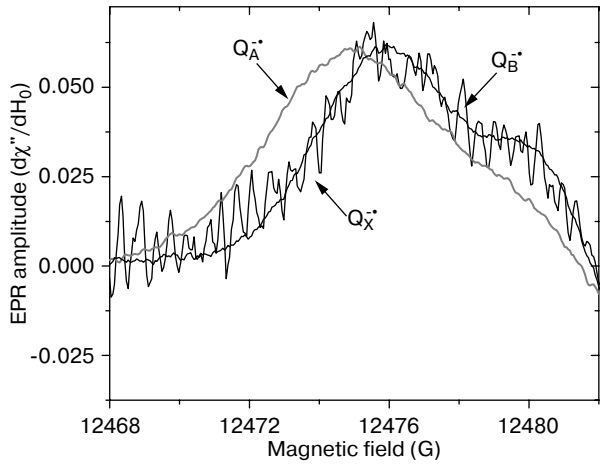

Fig. 7. EPR difference spectrum in the semiquinone region associated with $Q_X^{-\bullet}$. The $Q_A^{-\bullet}$ contribution to the observed spectrum (I = 2%) was removed as described in the text. The spectra for $Q_A^{-\bullet}$ (grey line) and $Q_B^{-\bullet}$ (black line) are shown for comparison. The difference spectrum of $Q_X^{-\bullet}$ matches that of the $Q_B^{-\bullet}$. This indicates that the component that gives rise to the slow phase is $Q_B^{-\bullet}$. (Conditions, same as for Fig. 6.)

was subtracted from the observed spectrum to give the deconvoluted spectrum shown in Fig. 7. The spectrum of $Q_X^{-\bullet}$ is compared with that of $Q_A^{-\bullet}$ and $Q_B^{-\bullet}$ in Fig. 7. The $Q_X^{-\bullet}$ spectrum best matches that of $Q_B^{-\bullet}$. This shows that the slow kinetic phase involves the formation of $Q_B^{-\bullet}$.

3.4 Light Saturation and Quantum Yield

The slow rise kinetics seen for the new signal (Figs. 3–5) suggests a low quantum yield for its formation. In order to measure the quantum yield for the formation the light saturation behavior of the signal was studied. For the light-induced charge separation under steady-state illumination, the fraction of RCs in the charge-separated state at a given light intensity depends on the competition between the rate of formation and the rate of decay. The former depends upon the quantum yield for electron transfer to form the charge-separated state and the latter depends upon the recombination rate constant. The light intensity dependences of the amplitudes of the fast and slow phases (attributed to $D^{+\bullet}Q_A^{-\bullet} \rightarrow DQ_A$ and $D^{+\bullet}Q_B^{-\bullet} \rightarrow DQ_B$, respectively) are shown normalized in Fig. 8. The amplitude of the slower component saturated at lower light intensity than that of the faster decaying component. This explains why the relative amplitude of the two phases was dependent on the light intensity. The reason for the difference in saturation behavior was due to the longer lifetime of the new signal (6 s compared to 0.03 s) that more than compensates for its lower quantum yield of formation. A model was used to fit the observed light intensity

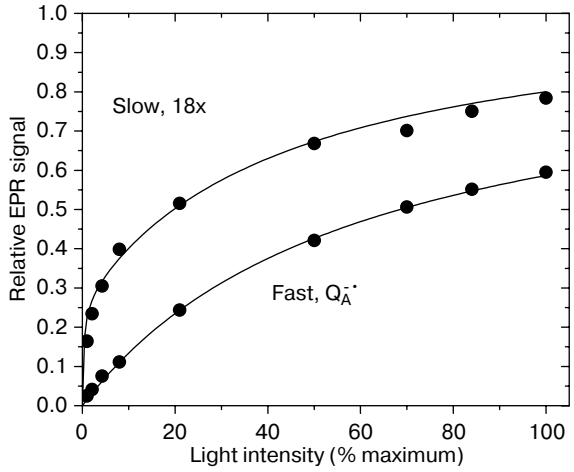

Fig. 8. Amplitudes of the slow and fast components as a function of the light intensity (plotted as a percentage of maximal). The amplitudes were normalized to 1.0 at infinite light intensity. This resulted in an 18-fold increase in the relative amplitude of the slow component, which is smaller than that of the fast at all light intensities; it had a value near 5% at $I = 100\%$. The fast-phase amplitude was fitted by Eq. (6) to obtain the value of σ. Equation (8) was used to fit the slow-phase data using a heterogeneous distribution of two RC fractions capable of B branch transfer: a large fraction ($\alpha_1 = 15\%$) with low quantum yield ($\Phi_{B_1} = 0.2\%$) and a smaller fraction ($\alpha_2 = 1.5\%$) with high quantum yield ($\Phi_{B_2} = 100\%$).

dependence to obtain the quantum yields (see appendix). In this model most of the RCs ($1-\alpha$) can only undergo electron transfer to Q_A with a quantum yield of $\Phi_A = 0.98$ [19] and a small fraction (α) of RCs can also undergo electron transfer to Q_B with quantum yield Φ_B (see appendix). The value of the cross-section σ was obtained by fitting the saturation behavior of the fast-decaying component by Eq. (6). The slowly decaying component could not be adequately described by a one-component fit (Eq. (7)) but could be well represented by a two-component fit (Eq. (8)). The two features that had to be modeled were the sharp increase in signal amplitude at low intensity and the more gradual increase at higher light intensity (Fig. 8). The quantum yields for the two components were constrained to values of 0.2% observed previously in mutant RCs [33] and 100% for RCs frozen under illumination. With these two constraints the model consisted of a larger fraction ($\alpha_1 = 15\pm5\%$) with lower quantum yield ($\Phi_{B_1} = 0.2\%$) and a smaller fraction ($\alpha_2 = 1.5\pm0.5\%$) with higher quantum yield ($\Phi_{B_2} = 100\%$). Despite its higher abundance, the low quantum yield component did not make a concomitant contribution to the observed $Q_B^{-\bullet}$ signal since it preferentially forms $Q_A^{-\bullet}$. In contrast, the small component with higher quantum yield preferentially formed $Q_B^{-\bullet}$.

4 Discussion

In this work we showed that in native RCs at cryogenic temperatures, a small fraction of the light-induced EPR signal (5%) formed upon continuous illumination, decayed more slowly ($\tau \sim 6$ s) than that observed previously for the $D^{+\bullet}Q_A^{-\bullet}$ state ($\tau = 30$ ms). The longer lifetime was characteristic of charge recombination from $D^{+\bullet}Q_B^{-\bullet}$ measured in RCs lacking Q_A. The amplitude of this phase was essentially eliminated when Q_B was displaced by the inhibitor stigmatellin. Furthermore, the EPR spectrum ($\nu = 35$ GHz) showed that the acceptor group had the spectrum (e.g. principal g-values) characteristic of $Q_B^{-\bullet}$. These results showed that $D^{+\bullet}Q_B^{-\bullet}$ was formed in the native RC at cryogenic temperatures. The light saturation data was fit to a simple model with two components capable of forming $D^{+\bullet}Q_B^{-\bullet}$, a larger component (15%) with a quantum yield of 0.2% and a smaller component (1.5%) with a quantum yield of 100%. We discuss below two possible mechanisms for this electron transfer process.

4.1 Photochemical Electron Transfer from $Q_A^{-\bullet}$ to Q_B at Cryogenic Temperature

The predominant mechanism for reduction of Q_B in native RCs involves the initial formation of the charge-separated state $D^{+\bullet}Q_A^{-\bullet}Q_B$ followed by electron transfer to form $D^{+\bullet}Q_AQ_B^{-\bullet}$:

$$DQ_AQ_B \rightarrow D^{+\bullet}Q_A^{-\bullet}Q_B \rightarrow D^{+\bullet}Q_AQ_B^{-\bullet}. \quad (2)$$

The second step in this reaction $k_{AB}^{(1)}$ is temperature dependent and is believed to be blocked at cryogenic temperatures [23, 24]. However, the $k_{AB}^{(1)}$ reaction does occur at cryogenic temperature in RC frozen under illumination [24–26]. This behavior has been explained as an example of conformational gating where a specific active protein conformation, similar to the product charge-separated state, is required for electron transfer. The active configuration is thus locked in by freezing in the charge-separated state.

In our results we found a small component of the RCs ($\alpha_2 = 1.5\%$) capable of forming $Q_B^{-\bullet}$ at low temperature with a quantum yield near 100%. One explanation for this component is that a small fraction of the RCs are in a conformation capable of electron transfer from $Q_A^{-\bullet}$ to Q_B at 80 K. The high quantum yield for this reaction is expected to be close to 100% since the quantum yield for electron transfer to form $D^{+\bullet}Q_A^{-\bullet}$ is about 100% and the activationless rate for the $Q_A^{-\bullet}Q_B \rightarrow Q_AQ_B^{-\bullet}$ reaction is expected to be about $10^9\ s^{-1}$ [39], much faster than the rate of the recombination reaction $D^{+\bullet}Q_A^{-\bullet} \rightarrow DQ_A$ ($30\ s^{-1}$). The lifetime of the $D^{+\bullet}Q_B^{-\bullet}$ from state observed here ($\tau \sim 6$ s) is different from the rates observed for RCs frozen under illumination, which have a wide distribution of recombination times from 10 s to $>10^7$ s [24–26]. This may be due to the different conditions during freezing, i.e., the native sample here was frozen in the

dark, while other samples were frozen under illumination. If this interpretation is correct, then a small fraction of RCs are in a configuration that is active for electron transfer at 80 K. Since this component is small (1.5%), we cannot yet rule out the possibility that this small fraction with high quantum yield is due to an unknown coincidental error. Further work needs to be done to further establish these results.

4.2 Photochemical Electron Transfer along the B Branch

The larger fraction of active RCs (15%) had a quantum yield of 0.2%, which is characteristic of B branch electron transfer (33). The most likely explanation for the electron transfer to Q_B observed here is that Q_B reduction occurs via B branch electron transfer in the native RC as shown by the following reaction:

$$DH_BQ_B \rightarrow D^{+\bullet}H_B^{-\bullet}Q_B \rightarrow D^{+\bullet}H_BQ_B^{-\bullet}, \tag{3}$$

where H_B is the intermediate bacteriopheophytin along the B branch (see Fig. 1). In the mutant RC in which Q_A is displaced by the Ala M260 $\rightarrow$ Trp mutation in the Q_A binding site, photochemical reduction of Q_B was observed at both room temperature [32] and 80 K [33]. Since this mutant had no changes to amino acid residues located along the B branch, we expect it to reflect the characteristics of B branch electron transfer in the native RC. At 80 K, the recombination (decay) time was 6 s [33], the same as was found for the slow-phase recombination in the present study. The quantum yield for Q_B reduction in the mutant RC ($\Phi = 0.2\%$) was also the same as that of the more abundant component in the present study. Thus, the characteristics of this fraction are the same as found for B branch electron transfer in a mutant RC in which A branch electron transfer to Q_B was eliminated. Therefore, we attribute the formation of $D^{+\bullet}Q_B^{-\bullet}$ in this larger fraction to B branch electron transfer observed in the native RC with a quantum efficiency of about 0.2%.

The small fraction (15%) of RCs that undergo Q_B reduction at 80 K by B branch electron transfer in the native RC is attributed to the specific conformational requirement for Q_B reduction. In previous studies with B branch mutant RCs at 80 K, about 30% of the RC sample could undergo charge separation to the $D^{+\bullet}Q_B^{-\bullet}$ state ($\tau = 6$ s). This result was explained by proposing that 30% of the RCs were in a conformation that was capable of electron transfer to Q_B; the major population of the RCs was in a conformation that was incapable of electron transfer to Q_B. Results from X-ray crystallography experiments indicate that the Q_B can occupy two primary binding sites. The proximal site is more polar with strong H bonds between the quinone ring and the His–Fe^{2+} and peptide amide protons [17] that can stabilize the electron on $Q_B^{-\bullet}$. The distal site is more hydrophobic with only one H bond between the quinone ring and a peptide backbone proton. Therefore, it was proposed that the minor population of RCs had Q_B in the proximal site, which favors Q_B reduction, and the majority in the distal site, which is less favorable for Q_B reduction. This interpretation is supported by the observation that Q_B in the crystal structure of the mutant RC was found predominantly in the distal site [31]. Additional support for this model came from ENDOR studies which show that in the active configuration, Q_B is in the proximal site [40]. Although infrared spectroscopic studies by Breton [41] at room temperature indicate that Q_B is mostly in the proximal site, the present results show that in about 15% of native RCs, Q_B is in an active configuration for B branch electron transfer, i.e, in the proximal configuration, at cryogenic temperatures.

It should be noted that overall yield for B branch transfer in native RC sample is very small (<1%) and electron transfer through this pathway is not likely to be biologically significant. However, its observation and understanding are of fundamental interest. Understanding differences in the quantum efficiencies of the two branches should provide fundamental information on the molecular basis for photochemical electron transfer and efficient solar energy conversion.

Appendix: Model of Quantum Yields for $Q_B^{-\bullet}$

The relative amplitudes of the fast and slow phases obtained following illumination can be modeled using a steady-state approximation in which the rate of formation of the charge-separated state is equal to the rate of its decay. This can be explained by the general reaction scheme depicted below, in which the formation rate constant is given by the absorption cross section σ, the quantum yield for electron transfer Φ and the light intensity I. The decay rate constant is k_{AD} and k_{BD} for recombination from $Q_A^{-\bullet}$ and $Q_B^{-\bullet}$, respectively. The results indicate a majority of RCs (fraction being equal to $1-\alpha$) lack a Q_B active in electron transfer. For this population applies

$$DQ_A \underset{k_{AD}}{\overset{k_{DA}=\sigma I\Phi_A}{\rightleftarrows}} D^{+\bullet}Q_A^{-\bullet}. \tag{4}$$

A small fraction, α, of RCs contain an active Q_B. For this population applies

$$D^{+\bullet}Q_AQ_B^{-\bullet} \underset{k_{DB}=\sigma I\Phi_B}{\overset{k_{BD}}{\rightleftarrows}} DQ_AQ_B \underset{k_{AD}}{\overset{k_{DA}=\sigma I\Phi_A}{\rightleftarrows}} D^{+\bullet}Q_A^{-\bullet}Q_B, \tag{5}$$

where the ground state can be converted to the charge-separated state by electron transfer to either Q_A or Q_B. At steady state the formation rate is equal to the decay rate and the ratio of RCs in the various charge-separated states relative to the ground state is equal given by the general equation

$$[D^{+\bullet}Q_i^{-\bullet}]/[DQ_i] = \sigma I\Phi_i\tau_{iD}, \tag{6}$$

where i = A or B for Q_A or Q_B, and $\tau_A = 1/k_{AD}$, $\tau_B = 1/k_{BD}$. The steady-state solution for the fraction of RCs having $Q_A^{-\bullet}$, and $Q_B^{-\bullet}$, $F_A(I)$ and $F_B(I)$, respectively, are given by the following equations:

$$F_A(I) = \frac{(1-\alpha)\sigma I \Phi_A \tau_{AD}}{\sigma I \Phi_A \tau_{AD} + 1} + \frac{\alpha \sigma I \Phi_A \tau_{AD}}{\sigma I \Phi_A \tau_{AD} + \sigma I \Phi_B \tau_{BD} + 1},$$

$$F_B(I) = \frac{\alpha \sigma I \Phi_B \tau_{BD}}{\sigma I \Phi_A \tau_{AD} + \sigma I \Phi_B \tau_{BD} + 1}. \quad (7)$$

The $F_B(I)$ is proportional to α and dependent on the relative values of quantum yields and decay times for $Q_A^{-\bullet}$ and $Q_B^{-\bullet}$. In order to fit the data, a heterogeneous distribution was used consisting of two forms of RCs capable of reducing Q_B at low temperature with different quantum efficiencies. The fraction of reduced Q_B for this distribution is

$$F_B(I) = \frac{\alpha_1 \sigma I \Phi_{B_1} \tau_{BD}}{\sigma I \Phi_A \tau_{AD} + \sigma I \Phi_{B_1} \tau_{BD} + 1} + \frac{\alpha_2 \sigma I \Phi_{B_2} \tau_{BD}}{\sigma I \Phi_A \tau_{AD} + \sigma I \Phi_{B_2} \tau_{BD} + 1}, \quad (8)$$

where Φ_{B_1} and Φ_{B_2} and α_1 and α_2 are the quantum yields and fractions of the first and second forms, respectively.

Acknowledgments

We thank George Feher, our friend and colleague, for his insight, guidance and good humor in over 30 years of research on magnetic resonance and photosynthesis. Supported by NIH grant GM41637 to M.Y.O.

References

1. Blankenship R.E.: Molecular Mechanisms of Photosynthesis. London: Blackwell Science Inc. 2002.
2. Hoff A.: Phys. Lett. **54**, 75–200 (1979)
3. Feher G.: Appl. Magn. Reson. **15**, 23–38 (1998)
4. Feher G., Okamura M.: Appl. Magn. Reson. **16**, 63–100 (1999)
5. Lubitz W., Feher G.: Appl. Magn. Reson. **17**, 1–48 (1999)
6. Bolton J., Clayton R., Reed D.: Photochem. Photobiol. **9**, 209–218 (1969)
7. Feher G.: Photochem. Photobiol. **14**, 373–387 (1971)
8. Leigh J., Dutton P.: Biochem. Biophys. Res. Commun. **46**, 414–421 (1972)
9. Norris J., Uphaus R., Crespi H., Katz J.: Proc. Natl. Acad. Sci. USA **68**, 625–628 (1971)
10. Feher G., Hoff A., Isaacson R., Ackerson L.: Ann. N. Y. Acad. Sci. **244**, 239–259 (1975)
11. Loach P.A., Hall R.L.: Proc. Natl. Acad. Sci. USA **69**, 786–790 (1972)
12. Okamura M.Y., Isaacson R.A., Feher G.: Proc. Natl. Acad. Sci. USA **72**, 3491–3495 (1975)
13. Butler W.F., Calvo R., Fredkin D.R., Isaacson R.A., Okamura M.Y., Feher G.: Biophys. J. **45**, 947–973 (1984)
14. Wraight C.A.: FEBS Lett. **93**, 283–288 (1978)
15. McElroy J., Mauzerall D., Feher G.: Biochim. Biophys. Acta **333**, 261–277 (1972)

16. Feher G., Isaacson R.A., Ackerson L.C., Okamura M.Y.: Biochim. Biophys. Acta **368**, 135–139 (1974)
17. Stowell M.H., McPhillips T.M., Rees D.C., Soltis S.M., Abresch E., Feher G.: Science **276**, 812–816 (1997)
18. Kirmaier C., Holten D.: Photosynth. Res. **13**, 225–260 (1987)
19. Wraight C., Clayton R.: Biochim. Biophys. Acta **333**, 246–260 (1974)
20. Wraight C.: Front. Biosci. **9**, 309–337 (2004)
21. Mulkidjanian A., Kozlova M., Cherepanov D.: Biochem. Soc. Trans. **33**, 845–850 (2005)
22. Vermeglio A., Clayton R.K.: Biochim. Biophys. Acta **461**, 159–165 (1977)
23. Chamorovsky S., Remennikov S., Kononenko A., Venediktov P., Rubin A.: Biochim. Biophys. Acta **430**, 62–70 (1976)
24. Xu Q., Gunner M.: Biochemistry **40**, 3232–3241 (2001)
25. Kleinfeld D., Okamura M.Y., Feher G.: Biochemistry **23**, 5780–5786 (1984)
26. Utschig L., Thurnauer M., Tiede D., Poluektov O.: Biochemistry **44**, 14131–14142 (2005)
27. Graige M., Feher G., Okamura M.: Proc. Natl. Acad. Sci. USA **95**, 11679–11684 (1998)
28. Laible P., Kirmaier D., Holten D., Tiede D., Schiffer M., Hanson D. in: Photosynthesis: Mechanisms and Effects (Garab G., ed.), pp. 849–852. Dordrecht: Kluwer 1998.
29. de Boer A., Neerken S., de Wijn R., Permentier H., Gast P., Vijgenboom E., Hoff A.: Photosynth. Res. **71**, 221–239 (2002)
30. Wakeham M., Jones M.: Biochem. Soc. Trans. **33**, 851–857 (2005)
31. Paddock M., Chang C., Xu Q., Abresch E., Axelrod H., Feher G., Okamura M.: Biochemistry **44**, 6920–6928 (2005)
32. Wakeham M., Goodwin M., McKibbin C., Jones M.: FEBS Lett. **540**, 234–240 (2003)
33. Paddock M.L., Flores M., Isaacson R., Chang C., Abresch E.C., Selvaduray P., Okamura M.Y.: Biochemistry (2006) in press
34. Paddock M.L., Rongey S.H., Abresch E.C., Feher G., Okamura M.Y.: Photosynth. Res. **17**, 75–96 (1988)
35. Debus R.J., Feher G., Okamura M.Y.: Biochemistry **25**, 2276–2287 (1986)
36. Utschig L., Greenfield S., Tang J., Laible P., Thurnauer M.: Biochemistry **36**, 8548–8558 (1997)
37. Flores M., Isaacson R., Abresch E., Calvo R., Lubitz W., Feher G.: Biophys J. **90**, 3356–3362 (2006)
38. Oettmeier W., Godde D., Kunze B., Höfle G.: Biochim. Biophys. Acta **807**, 216–219 (1985)
39. Calvo R., Abresch E., Bittl R., Feher G., Hofbauer W., Isaacson R., Lubitz W., Okamura M., Paddock M.: J. Am. Chem. Soc. **122**, 7327–7341 (2000)
40. Paddock M.L., Isaacson R., Chang C., Feher G., Okamura M.Y.: Biophys. J. **86**, 11a (2004)
41. Breton J.: Biochemistry **43**, 3318–26 (2004)

Authors' address: Melvin Y. Okamura, Department of Physics, University of California, San Diego, La Jolla, CA 92093-0354, USA
E-mail: mokamura@ucsd.edu